GEOPHYSICS, VOL. 71, NO. 5 (SEPTEMBER-OCTOBER 2006); P. H55–H65, 11 FIGS.
10.1190/1.2235876

Tomographic imaging of permafrost using three-component seismic cone-penetration test

Anne-Marie LeBlanc[1], Richard Fortier[1], Calin Cosma[2], and Michel Allard[3]

ABSTRACT

We conducted seismic cone-penetration tests (SCPT) and tomographic imaging in a permafrost mound in northern Quebec, Canada, to study the cryostratigraphy and assess the seismic properties of permafrost at temperatures near 0°C. A swept impact source generating both P- and S-waves and penetrometer-mounted three-component accelerometers were used to acquire surface-to-depth first-arrival times as input to produce 2D images of P- and S-wave velocities. Based on the three-component accelerometer records and the propagation modes of body waves, the P- and S-wave first arrivals were detected and discriminated. The inversion of the first-arrival times was based on the simultaneous iterative reconstruction technique. The multioffset surface-to-depth geometry used in this study limits the lateral resolution of tomographic imaging. However, the vertical variation in seismic velocities in the permafrost mound shows good reproducibility and can be compared to the cone data. The gathering of cone data such as cone resistance, friction ratio, electrical resistivity, and temperature, along with the seismic velocities, provides new insights into the cryostratigraphy of permafrost. While the cone data are affected by the vertical heterogeneity because of the complex sequence of ice lenses and frozen soil layers of a few centimeters thickness, the smooth velocity variations of P- and S-waves characterized by a wavelength of a few meters depend on the bulk physical properties of permafrost. The P- and S-wave velocities varied from 2400 to 3200 m/s and from 850 to 1750 m/s, respectively, for a temperature range between 0°C and −2°C. At this temperature range, the variations in unfrozen water content are important and affect directly the seismic properties of permafrost. The decrease in P- and S-waves velocities in depth with the permafrost mound depends nonlinearly on the increase of unfrozen water content from 9% to 30% for a temperature increase from −2°C to 0°C.

INTRODUCTION

Permafrost is ground, either rock or sediment, that remains at or below 0°C for at least two years (ACGR, 1988). Permafrost zones occupy up to 24% of the exposed land area of the Northern Hemisphere (Zhang et al., 2001). Permafrost has received much attention recently because thawing and degradation are already occuring in discontinuous permafrost zones following climate warming in high latitudes (Romanovsky et al., 2002). The thawing of permafrost and thaw subsidence of ice-rich permafrost can affect directly the performance of manmade infrastructure by increasing maintenance cost, decreasing useful life span, and jeopardizing security. The delineation of permafrost zones and assessment of the physical properties of permafrost are therefore a major concern when engineering for infrastructure design and construction in cold regions. Geophysical surveys, particularly seismic surveys such as seismic refraction and reflection surveys, seismic logging, vertical seismic profiling (VSP), and seismic tomography, can be very useful to not only study the occurrence of permafrost but also to assess the properties of permafrost.

Seismic properties of frozen soils

The presence of ice in soils directly affects their seismic properties and causes a large increase in stiffness and seismic velocities be-

Manuscript received by the Editor May 12, 2004; revised manuscript received July 19, 2005; published online August 28, 2006.
[1]Centre d'études nordiques, Université Laval, Sainte-Foy, Québec, Canada G1K 7P4 and Département de géologie et génie géologique, Université Laval, Sainte-Foy, Québec, Canada G1K 7P4. E-mail: anne-marie.leblanc.1@ulaval.ca; richard.fortier@ulaval.ca.
[2]Vibrometric OY, Sitratori 3, 00420, Helsinki, Finland. E-mail: calin.cosma@vibrometric.com.
[3]Centre d'études nordiques, Université Laval, Sainte-Foy, Québec, Canada G1K 7P4 and Département de géographie, Université Laval, Sainte-Foy, Québec, Canada G1K 7P4. E-mail: Michel.Allard@cen.ulaval.ca.

cause pure ice has high P- and S-wave velocities of 3700 and 1800 m/s, respectively. In comparison, velocities in unfrozen soils are typically less than 2400 and 1100 m/s, respectively. Decreasing temperature and unfrozen water content lead to an increase in seismic velocities. The relative increase in P-wave velocity as the temperature decreases below 0°C is greatest for frozen, fine-grained soils (Nakano and Froula, 1973), but frozen, coarse-grained soils have higher seismic velocities than the fine-grained soils. The results of previous field and laboratory studies on seismic velocities of frozen soils are summarized and presented in LeBlanc et al. (2004). However, Vinson (1978) reported that there is a severe lack of seismic data between 0°C and –1°C.

Seismic studies in permafrost

Various researchers have carried out seismic refraction surveys in different cold environments for subsurface exploration and delineation of permafrost in the discontinuous permafrost zone (Barnes, 1963; Garg, 1973; Hunter, 1973; Hunter et al., 1978; MacAulay and Hunter, 1982; Morack and Rogers, 1982; Neave and Sellmann, 1983). For large-scale surveys applied to petroleum exploration and gas hydrate research in cold regions, the seismic reflection method is effective for imaging permafrost structures (Porturas, 1988; Skvortsov et al., 1992; Hunter et al., 1999; Miller et al., 2000).

Few case studies of seismic logging and VSP carried out in permafrost can be found in the literature. Wyder et al. (1972) used an uphole wavefront technique to investigate frozen unconsolidated materials. The P-wave first arrivals were detected with a linear array of geophones located at the surface away from the seismic source in a borehole. Hunter (1974) also tested the uphole wavefront technique for seismic logging in rock permafrost using a downhole geophone and a multiple source array at the surface. Skvortsov et al. (1992) have shown that seismic reflection and S-wave VSP carried out in permafrost can detect a massive ice body.

Seismic tomography has seen limited application to permafrost characterization. Bishop et al. (1984) assessed the spatial variation in seismic velocities in permafrost using a tomographic imaging approach. More recently, Gonzalez-Serrano et al. (1998) produced 3D seismic velocity models of permafrost for depth migration using seismic tomography. They showed that the results from seismic tomography can attenuate the distortions in reflections observed in seismic data because of the high contrast between frozen and unfrozen ground velocities.

Seismic logging or near-surface VSP can be carried out during a seismic cone-penetration test (SCPT) using penetrometer-mounted seismic receivers instead of lowering the receivers in a borehole. This eliminates all problems with the tube-waves and results in higher quality data while retaining all of the benefits of VSP (Jarvis and Knight, 2000). The decrease in the investigation cost in comparison to drilling a borehole, better acoustic coupling, and the gathering of cone data along with the seismic data are additional advantages (Jarvis and Knight, 2000).

Detailed descriptions and results of SCPT carried out in unconsolidated soils can be found in Robertson et al. (1986), Campanella and Stewart (1992), and Sully and Campanella (1992, 1995). Different seismic sources can be used to generate separate P- and S-waves. However, the use of an S-wave seismic source is preferred for geotechnical applications because the shear strength — a fundamental parameter for the design of foundations — can be assessed from the S-wave velocity. Only one offset between the seismic source at the surface and the SCPT normally is used to perform the seismic logging for geotechnical application.

The cone data such as cone resistance, friction ratio, pore pressure, and temperature measured during a cone-penetration test (CPT) in unconsolidated soils or gathered along with the seismic velocities during SCPT, are widely used to assess the soil stratigraphy, behavior, and some fundamental mechanical properties of soils (Campanella et al., 1984). Cone-penetration tests have also been carried out in frozen soils and permafrost (Ladanyi, 1976, 1985; Campanella et al., 1984; Ladanyi and Huneault, 1989; Ladanyi et al., 1991, 1995; Buteau and Fortier, 2000; Buteau, 2002), but without using the seismic capabilities of CPT.

In the research presented herein, researchers conducted SCPTs in a permafrost mound in northern Quebec, Canada, to study the cryostratigraphy and assess the seismic properties of permafrost. However, instead of using only one offset as in the standard SCPT for unconsolidated soils, a multioffset surface-to-depth configuration was used to perform tomographic imaging. A swept impact seismic source generating both P- and S-waves was used near the surface. In addition, three-component accelerometers serving as the seismic receivers in depth were embedded in the penetrometer driven into the permafrost. To the best of our knowledge, no attempt has been made in the past to perform multioffset SCPT in unconsolidated soils or permafrost for tomographic imaging. The major contributions of this paper are (1) the study of the cryostratigraphy of permafrost using 2D images and vertical logs of P- and S-wave seismic velocities, (2) the improvement of the interpretation of tomographic imaging by correlating the vertical logs of P- and S-wave seismic velocities with the stratigraphic profiles of cone data, and (3) the assessment of the dependencies of P- and S-wave velocities on temperatures near 0°C and unfrozen water content. The field methodology and the SCPT results including examples of P- and S-wave seismograms, 2D images and vertical logs of P- and S-wave seismic velocities, and stratigraphic profiles of cone date, are reported herein.

STUDY SITE AND FIELD METHODOLOGY

Study site

The fieldwork was conducted on the east coast of Hudson Bay, near the Inuit community of Umiujaq (56°N, 76°W) in northern Quebec, Canada, in the discontinuous and scattered permafrost zone. The study site is located in a valley leading to the north end of Guillaume-Delisle Lake. Because this valley was submerged by the postglacial marine transgression of the Tyrell Sea, the dominant Quaternary sediment overlying the valley floor is thick marine silty sand, a frost-susceptible material. Following the postglacial land uplift and the contact of marine sediments with the cold subarctic air, ground freezing occurred. The formation of segregation ice and differential frost heaving in marine sediments created permafrost mounds scattered across the valley bottom. The permafrost mounds are a widespread ice-rich periglacial feature in the discontinuous permafrost zone in northern Quebec. They are characterized by an oval or approximately round shape, 3 to 4 m higher than the surrounding terrain, caused by the frost heaving and about 50 m in diameter. Their internal temperature is near 0°C, making the permafrost very sensitive to any change in surface conditions induced by man-made infrastructures or climate change.

One borehole was drilled to a depth of 4.6 m in the permafrost mound a few meters away from the SCPTs conducted at the study site. The active layer, less than 2 m thick, is the surficial layer of the permafrost mound that is subject to annual thawing and freezing. Below the active layer, the permafrost is ice rich — up to 50% in volume for an average density of 1750 kg/m^3. The permafrost base is about 22.5 m deep (Fortier and Allard, 1998; Buteau, 2002). At a depth of 7 m, the ground temperature is −1.5°C. Below this depth, there is practically no annual fluctuation in ground temperature.

Surface-to-depth configuration

A cross-configuration of 40 shotpoints 1 m apart at the surface was formed by two survey lines (lines A and B in Figure 1) of 20 shotpoints each; these survey lines were used to perform the surface-borehole tomography. The SCPT was conducted at the intersection of the survey lines. The researchers conducted two deep SCPTs 1 m from each other (SCPT1 and SCPT2 in Figure 1) and down to a depth of 24 m, running through the permafrost layer in the permafrost mound on June 13 and 16, 2001. Survey lines B_1B_1' and B_2B_2' of both cross-configurations overlapped, while the survey lines A_1A_1' and A_2A_2' were separated by an offset of 1 m (Figure 1).

Seismic cone-penetration test

The penetrometer used is a Vertek cone with a 10 cm^2 cross-sectional area of the tip base and a 60° cone angle, a 100 cm^2 friction sleeve, an electrical resistivity module, an inclinometer, a temperature sensor at the tip, and a module of triaxial accelerometers. The pushing system developed specifically for penetration rate-controlled SCPT in permafrost (Buteau and Fortier, 2000; Buteau, 2002) was used to carry out the SCPTs. The SCPTs were carried out at a constant penetration rate of 0.1 cm/s. Figure 2 shows a detailed schematic illustration of the field experiment.

Seismic source

The seismic source used in the present study is based on the swept impact seismic technique (SIST) developed by Park et al. (1996), which is a combination of the Vibroseis swept-frequency (Crawford et al., 1960; Anstey, 1994) and the Mini-Sosie multiimpact techniques (Barbier et al., 1976). The source used is the VIBSIST-20, designed and made by Vibrometric Oy.

The seismic signal produced by the swept impact source is a series of short pulses generated according to a deterministic coding scheme over a given interval in which the rate of impacts increases linearly with time. Low-power and high-frequency broadband seismic pulses, generating both P- and S-waves, are produced by this seismic source. Because the deterministic coding scheme is discontinuous, the decoding process of the seismic signal is accomplished by a "shift-and-stacking" procedure that is much simpler and quicker than crosscorrelation (Park et al., 1996). The coding scheme is monitored with an impact sensor, a signal source accelerometer, mounted on the seismic source (Figure 2). This technique provides a higher S/N ratio and better resolution than a conventional single-pulse technique. Each impact had a frequency content between 40 and 2000 Hz. In the field, the rate of impacts was swept from 8 to 25 impacts per second over a 10-s duration. The total number of impacts during a sweep varied between 125 and 135.

Seismograph

Researchers used a high-resolution engineering seismograph, StrataVisor NZ-24 from Geometrics, to record the seismic signals of the triaxial accelerometers (PC-3 in Figure 2). The sampling interval

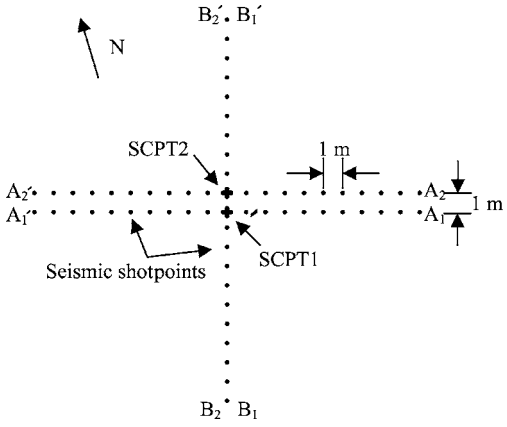

Figure 1. Adjacent cross-configurations of 40 seismic shotpoints for two SCPTs. The survey lines $B_1'B_1$ and $B_2'B_2$ were superposed while survey lines $A_1'A_1$ and $A_2'A_2$ were 1 m apart. The SCPT1 and SCPT2 were in the center of the cross-configurations.

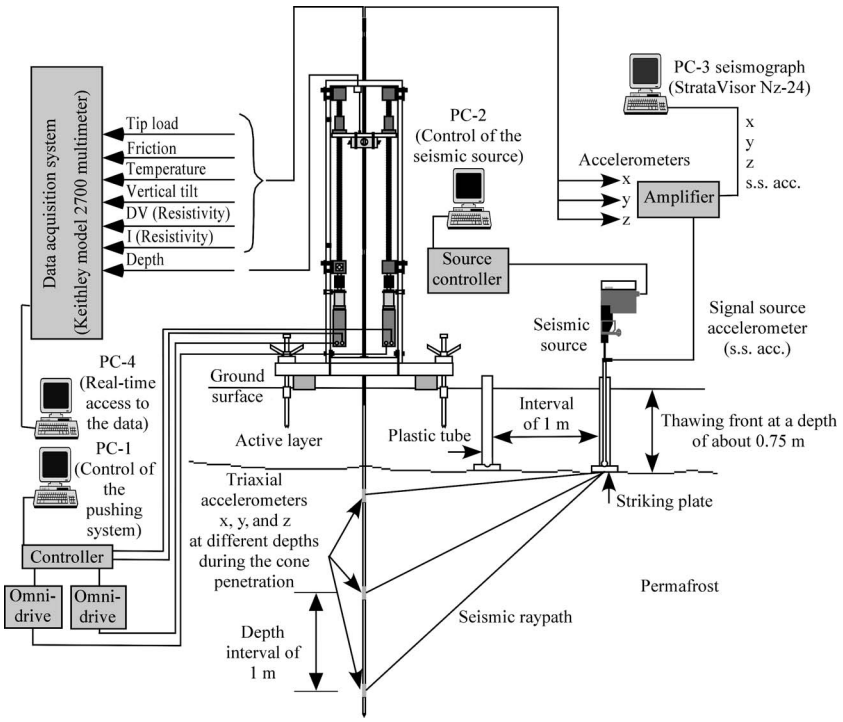

Figure 2. Schematic illustration of the field experiment (not to scale). Only three seismic receiver positions in depth and one seismic shotpoint near the ground surface are shown for clarity.

and the record length to monitor the seismic signal were 125 μs and 8.192 s, respectively. An initial delay of 2 s without recording was also used to stabilize the seismic source.

Seismic receivers

The seismic signal propagating in permafrost was recorded using a module of triaxial accelerometers embedded in the penetrometer. Accelerometers were preferred to geophones for monitoring the high-frequency seismic signal generated by the seismic source. The three orthogonal components, two horizontal (x and y) and one vertical (z), were oriented to approximately align the horizontal x-component with survey line A of shotpoints and the y-component with line B (Figures 1 and 3).

Field methodology

Cone resistance, friction load, temperature, cone inclination from the vertical, and electrical resistivity were measured by sensors embedded into the penetrometer and automatically recorded with a data acquisition system (Figure 2). From the surface down to a depth of 24 m, the cone penetration was stopped at depth intervals of 1 m to add a new pushing rod, perform the seismic shots with the seismic source following the cross-configuration (Figure 1), and record with the seismograph the seismic waves propagating down to the accelerometers embedded in the penetrometer. The seismic source stood directly on the thawing front at a depth of about 0.75 m in the active layer for a better mechanical contact and to avoid the signal attenuation in the unfrozen ground at the surface.

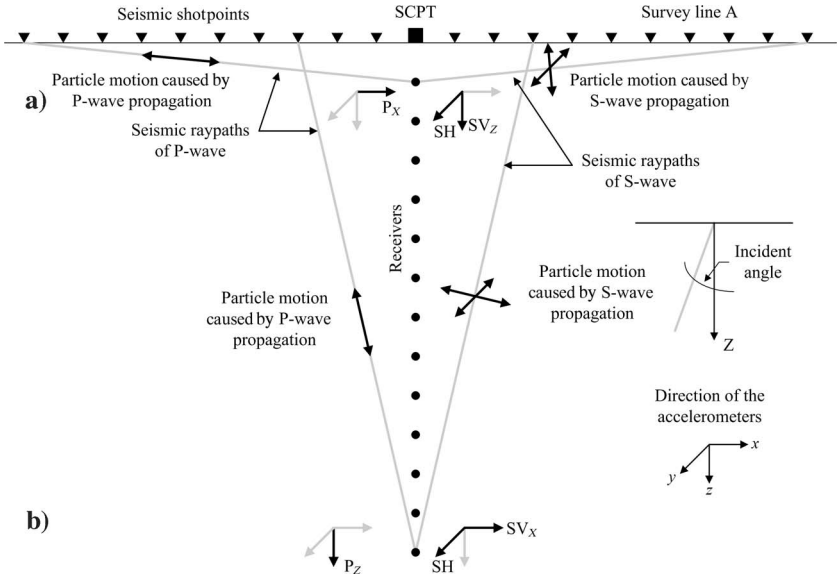

Figure 3. Influence of the incident angle of the seismic raypath on the triaxial accelerometers coupling response. Receivers X and Z lie on the source-receivers plane. The black arrows indicate which triaxial accelerometer has a good coupling and can detect a P-wave or an S-wave for two different incident angles: (a) a high incident angle and (b) a low incident angle. The components of the P-wave are P_X and P_Z. The S-waves are polarized and can be decomposed into two components: the component SV in the sources-receivers plane, which can be further decomposed into two other components SV_X and SV_Z, and the component SH, which is perpendicular to the sources-receivers plane.

SEISMIC DATA PROCESSING

The first step of data processing is to improve the quality of the signal source. A notch filter at 60 Hz was applied to the signal source because the signal source was affected by 60-Hz electrical noise from a power line. The record length and number of impacts N were also reduced in order to suppress the constant rate of impacts at the end of the sweep even with a carefully controlled impact sequence. Once the quality of the signal source was enhanced, we performed a summation of the pulses in the seismic records according to the shift-and-stacking procedure proposed by Park et al. (1996).

A fast Fourier transform applied to the decoded signals provided the power spectra. The frequency content of the body waves propagating in the permafrost varies typically between 200 and 1000 Hz. However, at depths greater than 22 m in the unfrozen ground below the permafrost base, the high frequencies were attenuated. According to the frequency content, a band-pass filter between 180 and 1000 Hz was used.

Initially, researchers used a correlation-based algorithm for automatic time picking of P- and S-wave first arrivals. Thereafter, manual time picking was systematically used to modify the first-arrival times on some seismic traces if necessary. The inversion of the first-arrival times based on the simultaneous iterative reconstruction technique (SIRT) algorithm (Gilbert, 1972) provided the 2D images of P- and S-wave seismic velocities. As a first approximation, an initial velocity model was created assuming straight raypaths. Then, starting with this initial velocity model, curved wave paths were computed iteratively during the tomographic inversion using a combination of a smoothing method for the coarse raypath estimates and a bending method for the refinement of the raypath (Um and Thurber, 1987). The medium is assumed to be isotropic.

The 2D discrete models representing the investigated medium were made of discrete elements or square cells. The size of the square cells was fixed at 1 m to respect the physical and mathematical resolutions of the problem. The cell size should be as close as possible to the wavelength. The wavelengths are approximately 4.1 and 2.5 m, respectively, for a P-wave dominant frequency of 700 Hz and an average velocity of 2900 m/s, and for an S-wave dominant frequency of 550 Hz and an average velocity of 1400m/s. However, the mathematical resolution function of the number of seismic raypaths in the model is the most important criterion. The number of cells should be kept below the number of raypaths. In the present case, 250 cells were used for a maximum number of 480 raypaths. Smooth models in the horizontal direction were considered in order to respect the horizontal structure of the permafrost layers. This smoothing procedure includes the choice of the number of cells and the weighting for the central cell.

Because the SIRT algorithm minimizes the difference between the synthetic traveltimes and the observed ones, all the tomographic images presented in this paper were selected for their smallest root mean square (rms) misfit between the observed and synthetic traveltimes. The residual mean squares used during the inversion process

are near 0.065 ms for the tomograms of P-wave velocities and near 0.090 ms for the tomograms of S-wave velocities. Furthermore, the models should be geologically reasonable. The cone data were used to correlate with the seismic velocities and check the quality of the tomographic images.

DISCRIMINATION OF FIRST ARRIVALS

In this study, the incident angle of a seismic raypath is defined relative to the vertical (or the vertical accelerometer Z), while the P- and S-wave components are defined relative to the vertical plane formed by the sources and receivers (Figure 3). In Figure 3, the horizontal accelerometer X and vertical accelerometer Z are in the sources-receiver plane, while the horizontal accelerometer Y is perpendicular to this plane. The P-wave can be separated into two components — the horizontal P_X-wave and the vertical P_Z-wave — both propagating in the sources-receiver plane. The horizontal component P_Y-wave is assumed to be negligible. The S-wave component in the sources-receiver plane is the SV-wave and can be seperated into two other components — the vertical SV_Z-wave and the horizontal SV_X-wave. The SH-wave is the horizontal component of the S-wave that is perpendicular to the sources-receiver plane (and is therefore in the Y direction).

The examples given herein of seismic traces (Figures 4, 5, and 7) were recorded along the survey line A of the tomographic imaging on June 16, 2001 (SCPT2 in Figure 1). The seismic traces are normalized to the maximum amplitude of each trace. The variations in relative amplitude are shown in the histogram on the right side of each set of seismic traces (Figures 4, 5, and 7). As expected, the signal amplitude decreases with the increase in the source-to-receiver distance.

Variation of the incident angle

For low incident angles or for deep receivers and/or small offset (Figure 3b), the particle motion longitudinal to the direction of P-wave propagation is almost parallel to the vertical accelerometer *Z* allowing a full coupling and detection. On the other hand, the particle motion polarized in the plane of the wavefront and transverse to the direction of S-wave propagation is almost in the same plane defined by the horizontal accelerometers *X* and *Y* allowing a full coupling and detection (Figure 3b). However, for a large incident angle or for shallow receivers and large offset (Figure 3a), the P-wave is only recorded with the horizontal accelerometer X in the sources-receiver plane, while the S-wave is only recorded with the vertical accelerometer Z and the horizontal accelerometer *Y* perpendicular to the sources-receiver plane. The coupling between the SH-wave and the horizontal accelerometer *Y* does not depend on the incident angle (Figure 3).

The traces of the first arrivals of the P_Z-wave for an offset of 1 m at 1-m depth intervals down to a depth of 24 m are shown in Figure 4a, while the traces of the SV_X-wave for an offset of 3 m are shown in Figure 4b. These two examples are representative of low incident angles where the P-wave and the SV-wave are most effectively monitored with the accelerometers *Z* and *X*, respectively. In Figure 4a, the raypaths between the source and receivers are almost vertical at greater depths. The SV-wave is therefore not detected by the vertical accelerometer *Z*, while the coupling between the P-wave and the vertical accelerometer *Z* is maximized. In Figure 4b, faint first arrivals associated with the P-wave are also detected because, even with a low incident angle and a particle motion almost perpendicular to the receiver, a small coupling still exists between the P-wave and the horizontal accelerometer *X*.

The seismic traces for the horizontal accelerometer *X* and an offset of 8 m are given in Figure 5a. The first-arrivals of the P-wave are detected because the particle motion is almost longitudinal to the direction of the horizontal accelerometer. Moreover, the first arrivals of the SV-wave become more apparent at depths greater than 8 m. Figure 5b shows the seismic traces recorded with the vertical accelerometer *Z* for the same offset of 8 m. This example illustrates the transition in first arrival detection on the vertical accelerometer *Z* from the SV-wave near the surface and the P-wave at greater depths. The transition zone where both the SV-wave and the P-waves are distinguishable on the same traces is close to an incident angle of 45°.

Change in polarization

The change in polarization of both P- and S-waves from one side to the other side of a survey line of tomography imaging centered on the SCPT allows the discrimination of body waves in the seismic

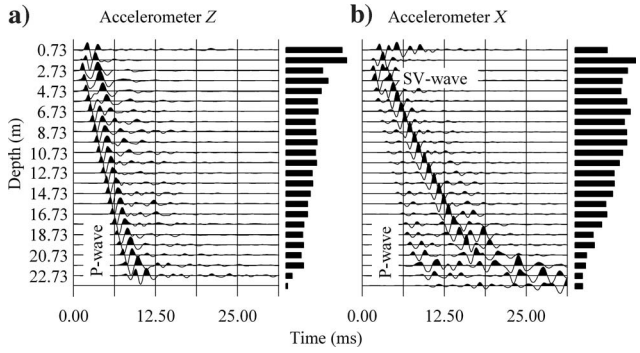

Figure 4. (a) Seismic traces showing mainly P-wave arrivals recorded with the vertical accelerometer *Z* at 1-m depth intervals down to a depth of 24 m and for a shotpoint on line A at an offset of 1 m from the SCPT2. (b) Seismic traces showing mainly SV-wave arrivals recorded with the horizontal accelerometer *X* at 1-m depth interval down to a depth of 24 m and for a shotpoint on line A at an offset of 3 m from the SCPT2.

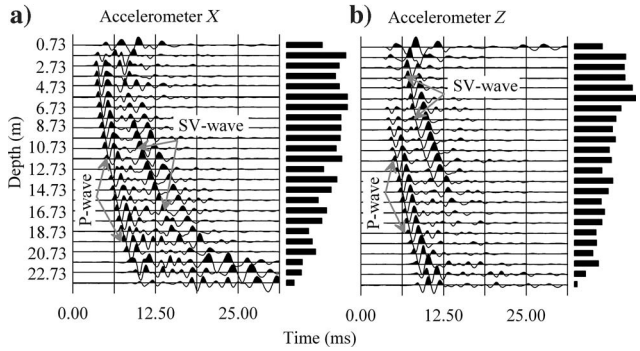

Figure 5. (a) Seismic traces showing P-wave and SV-wave arrivals in the sources-receiver plane recorded with the horizontal accelerometer *X*. (b) Seismic traces showing P-wave and SV-wave arrivals in the sources-receiver plane recorded with the vertical accelerometer *Z*. These traces are at 1-m depth intervals down to a depth of 24 m and for a shotpoint on line A at an offset of 8 m from the SCPT2.

traces (Figure 6). All seismic shots performed on one side of a survey line should have the same polarity. An inversion in polarity of the P_X-wave and SV_X-wave recorded with the horizontal accelerometer, *X*, occurs when the source is moved from one side to the other side of the survey line (Figure 6a and b). However, no inversion in polarity occurs for the P_Z-wave and SV_Z-wave recorded with the vertical accelerometer Z (Figure 6a and b).

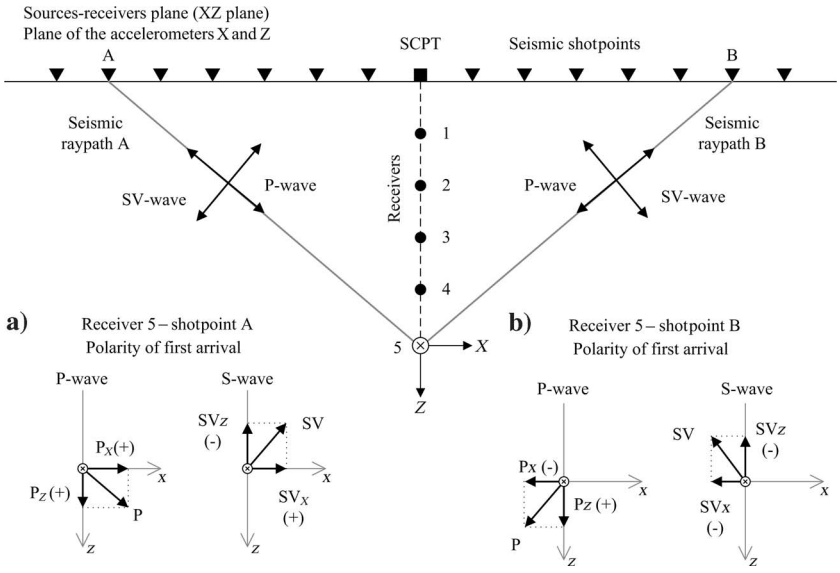

Figure 6. Vertical and horizontal decomposition in the sources-receiver plane of the P-wave and SV-wave first arrivals recorded with the accelerometers X and Z for two seismic raypaths. (a) The seismic raypath A is for a shotpoint A on the left side of the survey line relative to the SCPT. (b) The seismic raypath B is for a shotpoint B on the right side of the survey line relative to the SCPT. The polarity is indicated by the orientation of the vectors and the + and − symbols.

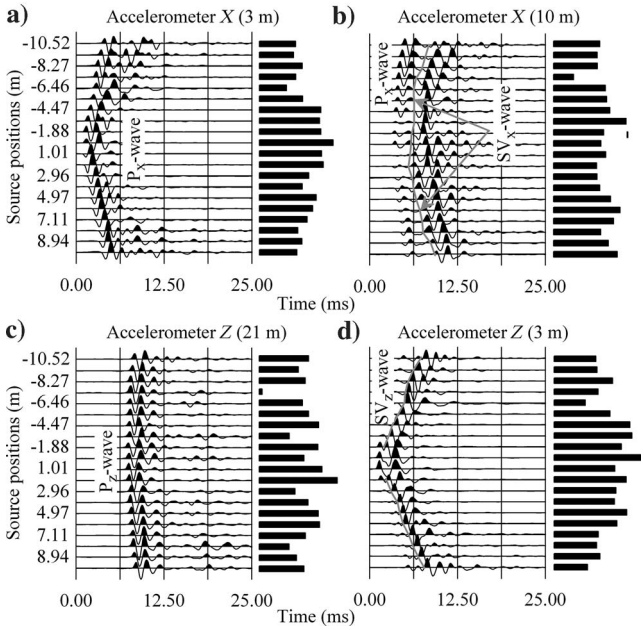

Figure 7. Seismic traces at 1-m offset interval from −10 to 10 m relative to the SCPT2 location along the survey line A. (a) Polarity inversion of the P_X-wave arrivals recorded with the horizontal accelerometer *X* at a depth of 3 m. (b) Polarity inversion of the SV_X-wave arrivals recorded with the horizontal accelerometer *X* at a depth of 10 m. (c) No polarity inversion of the P_Z-wave arrivals recorded with the vertical accelerometer *Z* at a depth of 21 m of the SCPT2. (d) No polarity inversion of the SV_Z-wave arrivals recorded with the vertical accelerometer *Z* at a depth of 3 m.

The four sets of seismic traces in Figure 7 are the examples of the four cases in Figure 6. For each set in Figure 7, the seismic traces are for a given depth and 20 source locations at 1-m offset interval from −10 to 10 m along the survey line, A, centered on the SCPT2. Figure 7a and b shows the seismic traces affected by an inversion in polarity of both the P_X-wave and the SV_X-wave, respectively, recorded with the horizontal accelerometer *X* at a depth of 3 and 10 m, respectively. Figure 7c and d shows the seismic traces of the P_Z-wave and the SV_Z-wave, respectively, without the inversion in polarity recorded with the vertical accelerometer *Z* at a depth of 21 and 3 m, respectively. In Figure 7b and d, the first arrivals of S-waves are marked with a gray line.

TOMOGRAPHIC IMAGES OF P- AND S-WAVES VELOCITIES

Twenty sets of 24 seismic traces (similar to the ones shown in Figures 4 and 5) per accelerometer and per survey line, representing 20 shotpoints along each survey line and 24 receivers at 1-m depth intervals down to a depth of 24 m, were used after data processing to pick the first arrivals, measure the traveltimes, invert the traveltimes as a function of the source-receiver locations, and compute the 2D images of P- and S-wave velocities. The tomographic image of P-wave velocity for the SCPT1 along the survey line A_1A_1' is given in Figure 8a while the image of S-wave velocity along the same line is given in Figure 9a. We computed the difference between two tomographic images to make easier the comparison between the survey lines A and B for SCPT1 and SCPT2 (Figure 1). For P- and S-waves respectively, the difference between SCPT1 and SCPT2 for the survey lines B is given in Figures 8b and 9b, and for the survey lines A in Figures 8c and 9c, while the difference between survey lines A and B of SCPT1 is given in Figures 8d and 9d. The seismic shotpoints on the thawing front are identified by triangle symbols, the SCPT location at the surface by a square symbol at a distance of zero, and the receivers in depth by dot symbols (Figures 8 and 9).

Because the raypath density is variable in the cells of the earth model, the image resolution is not uniform. The surface-to-depth configuration is most discriminating and accurate along the seismic shotpoint and receiver locations where the raypath density is greater than far away from these locations. Generally, for the 2D images of P- and S-wave velocities (Figures 8a and 9a), only one to fourteen raypaths intersect the boundary cells of the earth model. This small raypath density introduces artifacts of high velocities observed at the boundary cells. For the central cells, i.e., 2 to 3 m to either side of the SCPT, each cell is intersected by 30 to 55 raypaths with density increasing near the SCPT. However, increasing the number of raypaths cannot improve the resolution if the raypaths are restricted to a limited range of viewing angles. In the case of a surface-to-depth configuration, many cells are limited to a small viewing angle. The velocity resolution is better in the orientation parallel to the raypaths

(Shearer, 1999). Thus, for the experiments considered here, the vertical variation in seismic velocities is more significant than the horizontal one.

Keeping in mind the limitations of tomography, some observations can be made in Figures 8a and 9a on the lateral heterogeneity of the distribution of seismic velocities in the permafrost mound. Between 8 and 16 m deep, the left side of each tomographic image corresponding to the extremities A′ and B′ of the survey lines shows higher velocities, a difference of about 200 m/s and 300 m/s between each side is noted for P- and S-waves, respectively. In the field, these extremities are in the direction of the centre of the permafrost mound. Two other CPTs were carried out in the permafrost mound at the extremities of lines A_1' and A_2' but without using the seismic capabilities of CPT. Based on the stratigraphic information deduced from the four sets of cone data, the major layers are almost horizontal. Therefore, no major lateral changes in seismic velocities should be noted on the tomographic images. The difference in seismic velocities may be related to the cone inclination (Figure 10) inducing an error in the receiver locations and affecting the distribution of seismic velocities. The cone inclination reached a value of about 5° relative to the vertical at a depth of 24 m. No attempt was made to take into account this deviation from the vertical in the receiver locations because it is only an inclination relative to the vertical and the true orientation of inclination is unknown. Without correction, the seismic velocities are higher in the orientation of the cone inclination because the source-receiver distances are shorter in reality than the ones used in the tomographic inversion process. The traveltimes are also shorter than those for a perfectly vertical SCPT, thereby leading to higher seismic velocities.

The survey lines B_1B_1' and B_2B_2' of SCPT1 and SCPT2 overlap (Figure 1). The difference in seismic velocities must be negligible in theory (Figures 8b and 9b). This is the case for S-wave velocity with almost no difference except at the boundary cells (Figure 9b). On the other hand, we noted a difference in P-wave velocity between 0 and 200 m/s (Figure 8b). The survey lines A_1A_1' and A_2A_2' of SCPT1 and SCPT2 are 1 m apart (Figure 1). Like Figure 8b, Figure 8c shows a difference in P-wave velocity between 0 and 200 m/s except on the top right side of the tomographic image where the difference reaches −500 m/s. This anomaly in P-wave velocity is not perceptible for the S-wave (Figure 9c). However, differences in S-wave velocity of −500 m/s on the top left side and of 400 m/s on the middle left are noted in Figure 9c without equivalent anomalies in P-wave velocity (Figure 8c). These differences are probably inversion artifacts for both 2D images of P- and S-wave velocities, because a local variation in permafrost stiffness should result in anomalies in P- and S-wave velocities at the same region in the tomographic images. The cone inclination reached during SCPT2 was less than the one of SCPT1, but this difference in cone inclination alone cannot explain the anomalies in P- and S-wave velocities. Finally, Figures 8d and 9d show, for SCPT1, the anisotropy between survey lines A_1A_1' and B_1B_1'. In the case of the P-wave, there is no consistent evidence of anisotropy detected in Figure 8d, while Figure 9d presents a difference in S-wave velocity of 100 and 200 m/s on the left and right sides, respectively. Once again, because the anomalies in P- and S-wave velocities are not located in the same regions of the tomographic images, they are probably inversion artifacts, but may also be a result of anisotropy in permafrost stiffness along the two perpendicular survey lines A_1A_1' and B_1B_1'.

COMPARISON BETWEEN GEOTECHNICAL AND SEISMIC LOGS

The stratigraphy of the permafrost mound has been defined in terms of its mechanical, thermal, electrical, and seismic properties from the SCPT data. The results of the SCPT1 are given in Figure 10a. The results of SCPT2, not shown, are almost identical. In Figure 10b, four logs for both P- and S-wave velocities were calculated from the average velocity of two central cells along the SCPTs of tomographic images. From the variations in mechanical, thermal, and electrical properties in depth, a cryostratigraphic column can be deduced (Figure 10).

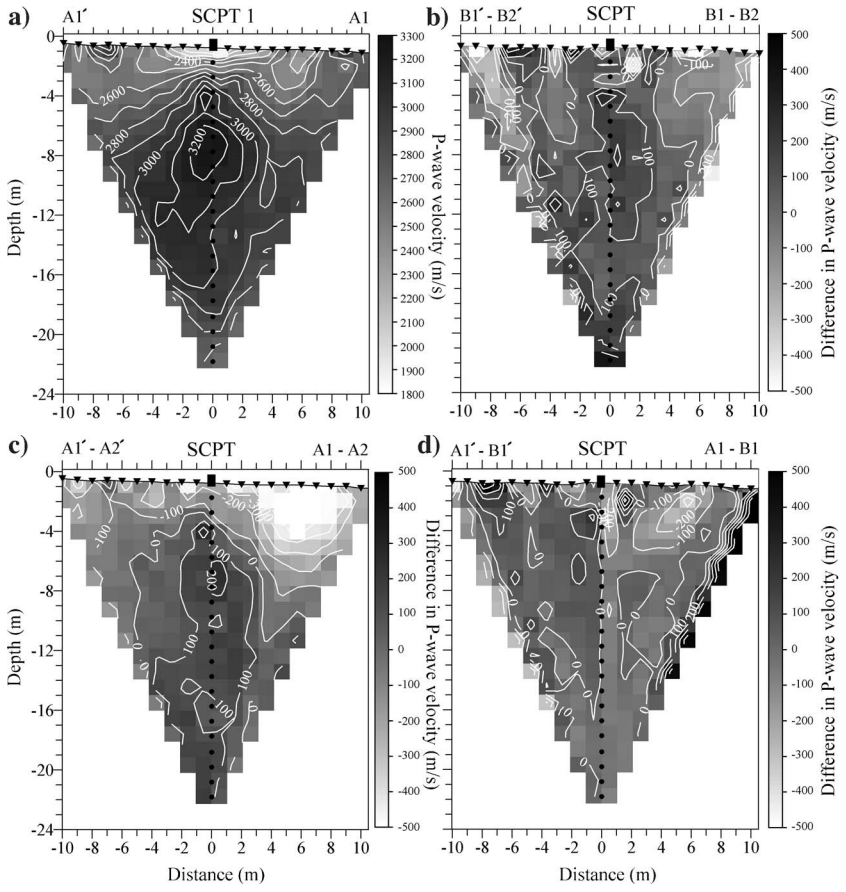

Figure 8. Tomograms of P-wave velocity. (a) Tomographic image carried out on June 13, 2001 (SCPT1), along line $A_1'A_1$. The computed differences between (b) the tomographic images carried out on June 13, 2001 (SCPT1), and on June 16, 2001 (SCPT2), along lines $B_1'B_1$ and $B_2'B_2$, (c) the tomographic image in (a) and the one carried out on June 16, 2001 (SCPT2), along line $A_2'A_2$ and (d) the tomographic image in (a) and the one carried out on June 13, 2001 (SCPT1), along line $B_1'B_1$.

The cone resistance q_c is a measure of the soil resistance to the cone penetration, while the friction ratio is a measure of the mobilized friction f_s along the friction sleeve of the penetrometer normalized by the cone resistance f_s/q_c. As a general interpretation rule of CPT in unfrozen ground, coarse-grained materials such as sand produce high cone resistance and low friction ratio, while fine-grained materials such as clay or silt produce low cone resistance and high friction ratio. According to previous studies of CPT in frozen ground (Campanella et al., 1984; Buteau, 2002), ice-rich permafrost and ice lenses are characterized by cone resistance in excess of 20 MPa and friction ratio lower than 1%. The permafrost table and permafrost base can be defined by the isotherm 0°C. The solid line in Figure 10 is the variation in depth of the dynamic temperature measured during the cone penetration. The friction along the penetrometer shaft warms up the penetrometer, as well as the surrounding soil, so the dynamic temperature does not reflect the in-situ conditions (Dlugach et al., 1995). The broken line is the temperature profile measured on June 16, 2001, using a thermistor cable permanently buried in the permafrost mound a few meters from the SCPT. Between 2 and 8 m, this profile is colder than the dynamic temperature, reaching −2°C at 3.5 m. However, the two curves are similar and they can be used together to locate the depth of the thawing front and the permafrost base. The electrical resistivity is measured during the cone penetration with the resistivity module of four electrodes spaced 3 cm apart following a Wenner array configuration. The electrical resistivity of frozen soils depends on the soil type, water salinity, unfrozen water and ice contents, cryostructure, and ground temperature. According to Fortier et al. (1993), the frozen fine silty sand is characterized by resistivity values over 1000 ohm-m with values as high as 100,000 ohm-m for an ice-rich layer. The last profile shown in Figure 10a is the cone inclination relative to the vertical. The seismic velocities in permafrost depend on the soil type, ground temperature, ice content, and unfrozen water content.

There are significant variations in cone resistance, friction ratio, and electrical resistivity with depth resulting from the complex sequence of frozen soil layers and ice lenses in the permafrost mound (Figure 10a). These variations occur at a scale of a few centimeters in depth. In comparison, the seismic profiles are much less variable (Figure 10b). As mentioned previously, the wavelength of P- and S-waves is on the order of few meters and at least two orders of magnitude larger than the complex sequence of frozen soil layers and ice lenses in permafrost. The seismic tomography is therefore completely blind to this small scale heterogeneity in permafrost. The P- and S-wave velocities depend only on the changes in bulk physical properties as a function of temperature in the permafrost mound. However, some important features can be highlighted in the SCPT profiles to assess the cryostratigraphy of the permafrost mound.

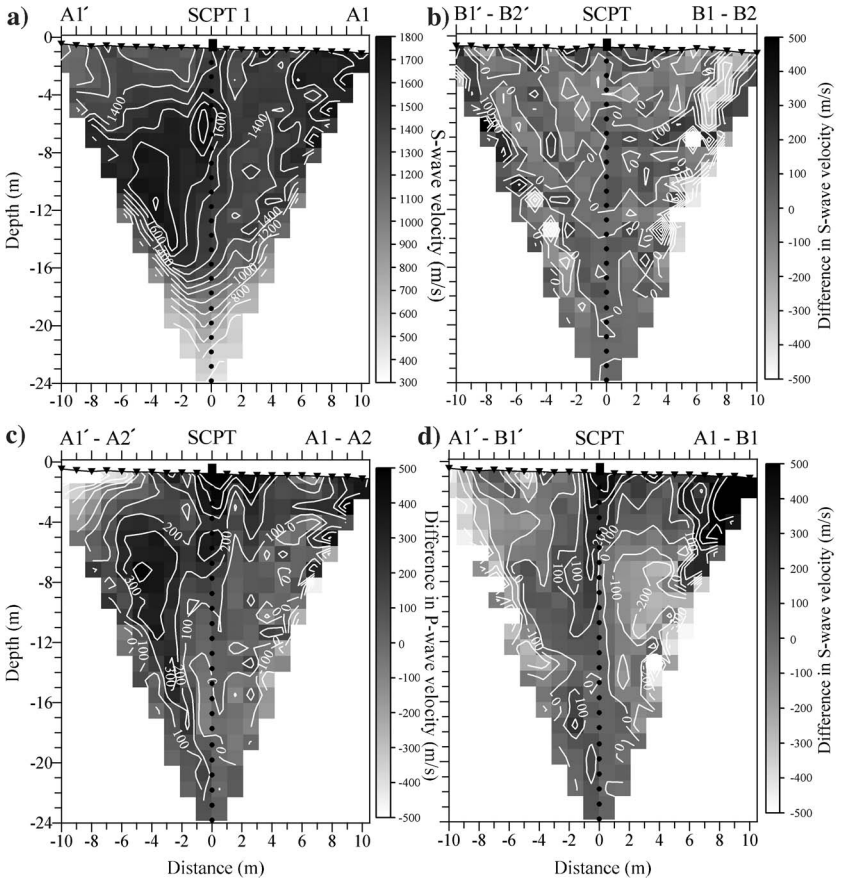

Figure 9. Tomograms of S-wave velocity. (a) Tomographic image carried out on June 13, 2001 (SCPT1), along line $A_1'A_1$. The computed differences between (b) the tomographic images carried out on June 13, 2001 (SCPT1), and on June 16, 2001 (SCPT2), along lines $B_1'B_1$ and $B_2'B_2$, (c) the tomographic image in (a) and the one carried out on June 16, 2001 (SCPT2), along line $A_2'A_2$ and (d) the tomographic image in (a) and the one carried out on June 13, 2001 (SCPT1), along line $B_1'B_1$.

In the middle of June 2001, the active layer was not completely thawed. The thawing front is clearly marked at a depth of 0.75 m by a sharp increase in cone resistance from few kPa in the thawed active layer up to 10 MPa in the frozen active layer, and an increase in friction ratio and electrical resistivity (Figure 10a). The permafrost table, the contact between the active layer and permafrost at a depth of about 1.7 m, is indicated by an increase in resistivity over the limit of 1000 ohm-m. The permafrost table is not highlighted clearly by a sharp increase in seismic velocities, but rather a gradual increase in velocities marks the passage between the frozen active layer and permafrost resulting from the decrease in ground temperature at depth (Figure 10b).

The ice-rich permafrost layers identified by the arrows in Figure 10a are characterized by very high values of cone resistance over 20 to 30 MPa, a low friction ratio below 1%, and high resistivity values in excess of 10,000 ohm-m. The seismic velocities in the permafrost range from 2400 to 3200 m/s for P-wave and from 850 to 1750 m/s for S-wave (Figure 10b). The maximum values of P- and S-wave velocities of about 3000 to 3200 and 1500 to 1750 m/s, respectively, occur between 6 and 7 m in depth where the ice content of permafrost is probably highest. An ice-rich layer of about 0.75 m thick just below 10 m in depth characterized by a high cone resistance of 30 MPa and electrical resistivity over 10,000 ohm-m is clearly identified. This thick ice-rich layer does not induce an increase in P- and S-wave velocities (Figure 10b). Another feature at a depth of about 13 m is also identified

in the SCPT profiles (Figure 10a). A few decimetres above 13 m, the low cone resistance associated with high friction ratios and low values of electrical resistivity suggests a thick layer of fine-grained soil with high unfrozen water content. Despite the fact that the thickness of this layer is lower than the tomographic resolution, this layer seems to be underlined by a slight decrease in P-wave velocity (Figure 10b) because the P-wave velocity is lower in water than in ice. However, the S-wave velocity is almost unaffected by this layer. Below 13 m, the variability of the cone resistance and the friction ratio is less significant, and the ice content is lower than above this depth. The ice-rich layers are also thinner because high values of cone resistance over 25 MPa are not noticed below 13 m, except at 17.8, 18.2, and 19.2 m in depth. These probably correspond to the last ice-rich layers (Figure 10a). Below 13 m, P- and S-wave velocities decrease slowly, probably caused by the increase in temperature and unfrozen water content and the decrease in ice content (Figure 10b).

At depths greater than 19.5 m, changes in ground conditions can be identified through a sharp decrease in electrical resistivity to values below 1000 ohm-m (Figure 10a). The permafrost base near 21.5 m is defined by the isotherm 0°C. Between 19.5 and 21.5 m in depth the ground is cryotic but unfrozen because the temperature is below 0°C and the resistivity is below 1000 ohm-m. The freezing point depression in this layer evaluated to about −0.5°C because of the overburden pressure (Fortier and Allard, 1998). Below the permafrost base, at a depth of 21.5 m, low values in S-wave velocity of about 500 m/s indicate the presence of unfrozen soil (Figure 10b). It is the perennially noncryotic ground.

The logs of P- and S-wave velocities are quite similar in general shape, reflecting the cryostratigraphy of the permafrost mound (Figure 10b). The profiles of P-wave velocity for survey lines A_1A_1' and B_1B_1' of SCPT1 (Figure 10b) are identical for depths greater than 3 m. As shown in Figures 8 and 9, no major azimuthal anisotropy in seismic velocities in the permafrost mound between the two seismic logs A_1A_1' and B_1B_1' is perceptible. However, the profiles of P-wave velocity for survey lines B_1B_1' and B_2B_2' of SCPT1 and SCPT2 (Figure 10b) have a systematic difference of about 200 m/s even though these two survey lines overlapped (Figure 1). This difference is close to the experimental error related to the sampling interval, the accuracy of picking the first arrivals and measuring the traveltimes, the penetrometer inclination from the vertical inducing an error in the receiver locations, and the raypath density and coverage used during the inversion process of traveltimes. The survey lines associated with SCPT1 show the higher velocity profiles, more evident for P-wave at depths greater than 3.5 m but also true for S-wave at depths greater than 6 m. Slight changes in surface conditions, progression of the thawing front, and warming of the active layer between the two SCPTs acquired 3 days apart may have affected the stiffness of permafrost and can explain the difference in the logs of P- and S-wave velocities near the surface. At depths greater than 6 m, the difference in S-wave velocity from one log to another is less than 200 m/s, and this difference is negligible below 12 m (Figure 10b). Overall, it is difficult to differentiate the experimental error from the changes in surface conditions because the trends from one log of P-wave or S-wave velocity to another are not the same for P- and S-wave velocities. However, the reproducibility of seismic logs is considered good.

The experimental nonlinear dependencies of P- and S-wave velocities on unfrozen water content are given in Figure 11 for the seismic logs of survey line B_2B_2' of SCPT2. The unfrozen water content of permafrost was deduced from a power-law relationship between

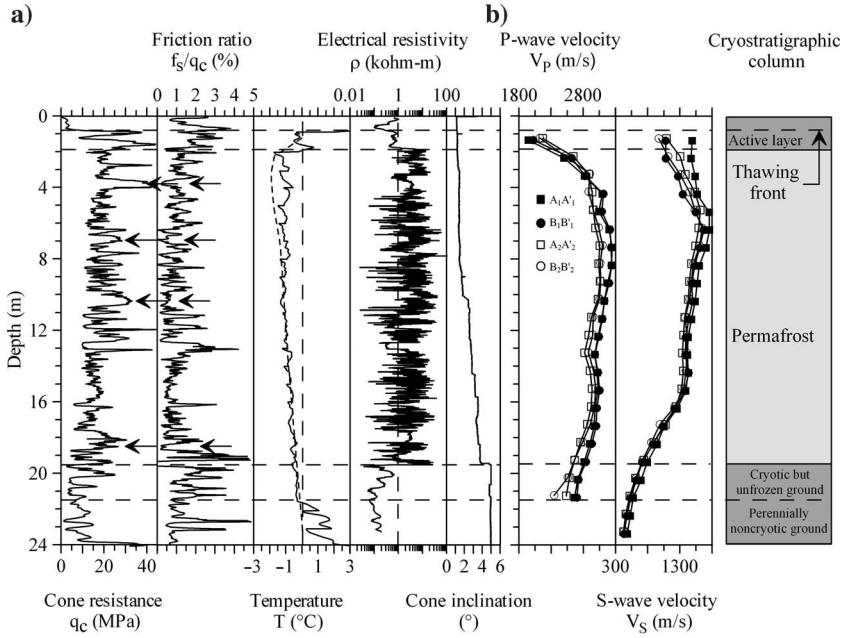

Figure 10. (a) Results of SCPT1 carried out on June 13, 2001. (b) Variation of P- and S-wave velocity with depth.

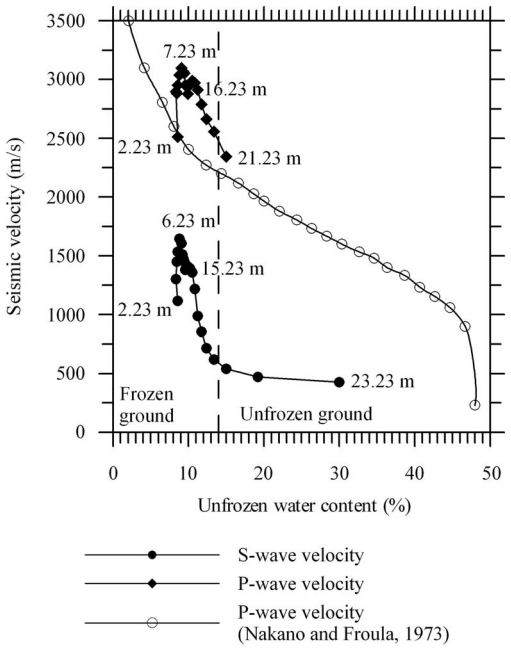

Figure 11. P- and S-wave velocities as a function of unfrozen water content.

the unfrozen water content and the temperature proposed by Fortier et al. (1996) for frozen silty sand. Fortier et al. (1996) measured directly in the field close to the study site the unfrozen water content of undisturbed permafrost samples using a calorimetric method. The temperature profile measured on June 16, 2001, on a thermistor cable was used to calculate the unfrozen water content. According to this empirical relationship, most of the increase in unfrozen water content occurs in the range of temperature between −2 °C and 0 °C. Below −2 °C, the unfrozen water content is almost constant at 8%. From near the surface to a depth of 7.23 or 6.23 m for P- and S-waves, respectively, the P- and S-wave velocities increase, while the unfrozen water content is nearly constant at 8%. The increase of the seismic velocities is explained by the variation of ice content with depth. From 7.23 or 6.23 m to 16.23 or 15.23 m in depth for P- and S-waves, respectively, the seismic velocities are near their maximum values, but they are affected by a small decrease as unfrozen water content increases slightly from 8% to 11%. Below 16.23 or 15.23 m, the P- and S-wave velocities decrease slowly because of the large increase in unfrozen water content near 0 °C, as the ground temperature increases slowly in depth following the geothermal gradient. At depths greater than 19.5 m and unfrozen water content higher than 14%, the seismic velocities do not vary significantly because the ground is unfrozen even if the temperature is still below 0 °C. For comparison purposes, the results of Nakano and Froula's (1973) laboratory tests conducted on artificially frozen clay are also given in Figure 11. However, no laboratory data are available for S-wave velocity.

CONCLUSIONS

A multioffset surface-to-depth geometry was used to perform seismic cone-penetration tests in a permafrost mound to conduct tomographic imaging, study the cryostratigraphy, and assess the seismic properties of permafrost at temperatures near 0 °C. A swept impact seismic source was moved near the surface to generate both P- and S-waves, and three-component accelerometers embedded in a penetrometer driven in depth in the permafrost mound were used to record the body waves propagating from the seismic source. The accuracy and reproducibility of vertical seismic logs defined from the 2D images of P- and S-wave velocities were adequate to delineate roughly the bulk physical properties of permafrost. However, the vertical resolution of the seismic logs is of the same order as the wavelengths of P- and S-waves (a few meters), simply not enough to detect the small scale heterogeneity of permafrost consisting of a complex sequence of ice lenses and frozen soil layers a few centimeters thick as shown by the cone data. Moreover, the surface-to-depth geometry is limited to a small viewing angle and is not well suited to studying the lateral variability of seismic properties in permafrost, especially at the boundary cells of the tomographic images. Therefore, the surface-borehole tomography is adequate for studying only the vertical variability of velocities of body waves in permafrost.

Cone data such as cone resistance, friction ratio, electrical resistivity, and temperature, along with the seismic data, provided useful information for characterizing permafrost without the cost of drilling a borehole. The CPT profiles showed the small scale heterogeneity of permafrost, while the seismic logs deduced from the tomographic images were characterized by smoothed curves indicating the bulk physical properties of permafrost. The cone resistance and friction ratio in permafrost varied mainly between 10 and 30 MPa and between 0% and 3%, respectively, with maximum values near 40 MPa and minimum values well below 1%, respectively, for ice-rich layers. The limit between unfrozen and frozen soil is clearly marked by the resistivity value of 1000 ohm-m. The P- and S-wave velocities varied from 2400 to 3200 m/s and 850 to 1750m/s, respectively, for a temperature range between 0 °C and −2 °C in permafrost. The empirical relationship between the seismic velocities and unfrozen water content for temperatures near 0 °C shows a general decrease in velocities with the increase in unfrozen water content. However, this relationship is more complex than the one established in the laboratory because of the variability in ice content and thermal conditions at depth. The nonlinear dependencies of P- and S-wave velocities on temperature and unfrozen water content found in the present study fill a knowledge gap in permafrost science.

ACKNOWLEDGMENTS

The authors would like to express their sincere gratitude to the Inuit community of Umiujaq and to Willie Kumarluk for their hospitality and friendly help during the field work. This research has been supported by the Natural Sciences and Engineering Council of Canada and by the Fonds de la recherche sur la nature et les technologies of the Province of Québec. The assistance in the field of the Centre d'études nordiques members and geological engineering students, is much appreciated. Finally, special thanks are given to Sylvie Buteau for her expertise on the use of the pushing system for the penetration rate-controlled cone-penetration test.

REFERENCES

ACGR (Associate Committee on Geotechnical Research), 1988, Glossary of permafrost and related ground-ice terms: National Research Council of Canada, Ottawa, Permafrost Subcommittee, Technical Memorandum 142.
Anstey, N. A., 1994, Vibroseis: Prentice Hall, Inc.
Barbier, M. G., P. Bondon, R. Mellinger, and J. R. Viallix, 1976, Mini-SOSIE for land seismology: Geophysical Prospecting, **24**, 518–527.
Barnes, D. F., 1963, Geophysical methods for delineating permafrost: 1st International Conference on Permafrost, 349–355.
Bishop, T. N., K. P. Bube, R. T. Cutler, R. T. Langlan, P. L. Love, J. R. Resnick, R. T. Shuey, D. A. Spindler, and H. W. Wyld, 1984, Tomographic determination of velocity and depth in laterally varying media: Geophysics, **50**, 903–923.
Buteau, S., 2002, Étude de l'affaiblissement du comportement mécanique du pergélisol au réchauffement: Ph.D. thesis, Université Laval.
Buteau, S., and R. Fortier, 2000, Penetration rate-controlled CPT in permafrost: 53rd Annual Conference of the Canadian Geotechnical Society, 1225–1235.
Campanella, R. G., P. K. Robertson, D. Gillespie, and E. J. Klohn, 1984, Piezometric-friction cone investigation at a tailing dam: Canadian Geotechnical Journal, **21**, 551–562.
Campanella, R. G., and W. P. Stewart, 1992, Seismic cone analysis using digital signal processing for dynamic site characterization: Canadian Geotechnical Journal, **29**, 477–486.
Crawford, J. M., W. Doty, and M. R. Lee, 1960, Continuous signal seismograph: Geophysics, **25**, 95–105.
Dlugach, A., A. Loktev, O. Okko, and S. Rokos, 1995, Soil mechanical properties and in situ temperature from arctic offshore CPT data: International Symposium on Cone-Penetration Testing, **2**, 167–172.
Fortier, R., and M. Allard, 1998, Induced polarization and resistivity logging in permafrost: 7th International Conference on Permafrost, 275–282.
Fortier, R., M. Allard, and M. K. Seguin, 1993, Effects of physical properties of frozen ground on electrical resistivity logging: Cold Regions Science and Technology **22**, 361–384.
Fortier, R., M. Allard, and F. Sheriff, 1996, Field estimation of water-ice phase composition of permafrost samples using a calorimetric method: Canadian Geotechnical Journal, **33**, 355–362.
Garg, O. P., 1973, In situ physicomechanical properties of permafrost using geophysical techniques: 2nd International Conference on Permafrost, 508–516.
Gilbert, P., 1972, Iterative methods for the 3D reconstruction of an object from projections: Journal of Theoretical Biology, **36**, 105–117.
Gonzalez-Serrano, A., A. Ramirez-Cuellar, J. Kapoor, D. Ince, T. P. Sum-

mers, and S. T. Michell, 1998, Refining 3D velocity models for depth migration using tomography: Application to rapid permafrost variations in Alaska's North Slope transition zone province: 68th Annual International Meeting, SEG, Expanded Abstracts, 1203–1206.
Hunter, J. A., 1973, The application of shallow seismic methods to mapping of frozen surficial materials: 2nd International Conference on Permafrost, 527–535.
———, 1974, Seismic uphole wavefront experiments in permafrost, Schefferville, Québec: Geological Survey of Canada, Paper 74–1, Part B, 83–86.
Hunter, J. A., R. D. Miller, W. E. Doll, B. J. Carr, R. A. Burns, R. L. Good, D. R. Laflem, M. Douma, and M. Riedel, 1999, Feasibility of high-resolution P- and S-wave seismic reflection to detect methane hydrate: 69th Annual International Meeting, Expanded Abstracts, SEG, 445–448.
Hunter, J. A., K. G. Neave, H. A. MacAulay, and G. D. Hobson, 1978, Interpretation of sub-seabottom permafrost in the Beaufort Sea by seismic methods. Part I, Seismic refraction methods: 3rd International Conference on Permafrost, 515–521.
Jarvis, K. D., and R. Knight, 2000, Near-surface VSP survey using the seismic cone penetrometer: Geophysics, **65**, 1048–1056.
Ladanyi, B., 1976, Use of the static penetration test in frozen soils: Canadian Geotechnical Journal, **13**, 95–110.
———, 1985, Use of the cone-penetration test for the design of piles in permafrost: Journal of Energy Resources Technology, **107**, 183–187.
Ladanyi, B., and P. Huneault, 1989, Cone-penetration tests in permafrost — The Fox Tunnel, Alaska: International Symposium on Mining in the Arctic, 75–82.
Ladanyi, B., T. Lunne, P. Vergobbi, and B. Lhuiller, 1995, Predicting creep settlements of foundations in permafrost from the results of cone-penetration tests: Canadian Geotechnical Journal, **11**, 835–847.
Ladanyi, B., T. Lunne, and W. Winsor, 1991, Experience with the performance of load-controlled cone-penetration test in permafrost and ice: 44th Canadian Geotechnical Conference, Reprint 1, Canadian Geotechnical Society, 41-1–41-8.
LeBlanc, A-M., R. Fortier, M. Allard, C. Cosma, and S. Buteau, 2004, Seismic cone-penetration test and seismic tomography in permafrost: Canadian Geotechnical Journal, **41**, 796–813.
MacAulay, H. A., and J. A. Hunter, 1982, Detailed seismic refraction of ice-bonded permafrost layering in the Canadian Beaufort Sea: 4th Canadian Permafrost Conference, 256–267.
Miller, R. D., J. A. Hunter, W. E. Doll, B. J. Carr, R. A. Burns, R. L. Good, D. R. Laflem, and M. Douma, 2000, Imaging permafrost with shallow P-wave and S-wave reflection: 70th Annual International Meeting, SEG, Expanded Abstracts, 1339–1342.
Morack, J. L., and J. C. Rogers, 1982, Marine seismic refraction measurements of near-shore subsea permafrost: 4th Canadian Permafrost Conference, 249–255.
Nakano, Y., and N. H. Froula, 1973, Sound and shock transmission in frozen soils: 2nd International Conference on Permafrost, 359–369.
Neave, K. G., and P. V. Sellmann, 1983, Seismic velocities and subsea permafrost in the Beaufort Sea: 4th International Conference on Permafrost, 894–898.
Park, C. B., R. M. Miller, D. W. Steeples, and R. A. Black, 1996, Swept impact seismic technique (SIST): Geophysics, **61**, 1789–1803.
Porturas, F., 1988, Reflection seismic exploration and data processing in cold regions: 5th International Conference on Permafrost, 1459–1465.
Robertson, P. K., R. G. Campanella, D. Gillespie, and A. H. Rice, 1986, Seismic SCPT to measure in situ shear wave velocity: ASCE Journal of the Geotechnical Division, **112**, 791–803.
Romanovsky, V., M. Burgess, S. Smith, K. Yoshikawa, and J. Brown, 2002, Permafrost temperature records: Indicators of climate change: EOS, Transactions, American Geophysical Union, **83**, 589–594.
Shearer, P. M., 1999, Introduction to seismology, inversion of traveltime data: Cambridge University Press.
Skvortsov, A. G., J. A. Hunter, G. G. Gorianinov, R. A. Burns, A. M. Tsarov, and S. E. Pullan, 1992, High-resolution shear-wave reflection technique for permafrost engineering applications: 62nd Annual International Meeting, SEG, Expanded Abstracts, 382–384.
Sully, J. P., and R. G. Campanella, 1992, In-situ shear wave velocity determination using seismic cone penetration for evaluating soil anisotropy: 10th World Conference on Earthquake Engineering, 1269–1273.
———, 1995, Evaluation of in situ anisotropy from crosshole and downhole shear wave velocity measurements: Géotechnique, **45**, 267–282.
Um, J., and C. Thurber, 1987, A fast algorithm for two-point seismic ray tracing: Bulletin of the Seismological Society of America, **77**, 972–986.
Vinson, T. S., 1978, Response of frozen ground to dynamic loading, *in* O. B. Andersland and D. M. Anderson, eds., Geotechnical Engineering for Cold Regions: McGraw-Hill Book Company, 405–458.
Wyder, J. M., J. A. Hunter, and V. Rampton, 1972, Geophysical investigations of surficial deposits at Tuktoyaktuk, N. W. T: Geological Survey of Canada, Open File 127.
Zhang, T., J. A. Heginbottom, R. G. Barry, and J. Brown, 2001, Further statistics on the distribution of permafrost and ground-ice in the Northern Hemisphere: Polar Geography, **24**, 126–131.